In-plane charged domain walls with memristive behaviour in a ferroelectric film

https://doi.org/10.1038/s41586-022-05503-5

Received: 29 November 2019

Accepted: 1 November 2022

Published online: 18 January 2023



Check for updates

Zhongran Liu^{1,9}, Han Wang^{2,3,9}, Ming Li^{4,9}, Lingling Tao⁴, Tula R. Paudel^{4,5}, Hongyang Yu¹, Yuxuan Wang¹, Siyuan Hong⁶, Meng Zhang⁶, Zhaohui Renˀ, Yanwu Xie⁶, Evgeny Y. Tsymbal⁴⊠, Jingsheng Chen^{2⊠}, Ze Zhang^{1,7⊠} & He Tian^{1,7,8⊠}

Domain-wall nanoelectronics is considered to be a new paradigm for non-volatile memory and logic technologies in which domain walls, rather than domains, serve as an active element. Especially interesting are charged domain walls in ferroelectric structures, which have subnanometre thicknesses and exhibit non-trivial electronic and transport properties that are useful for various nanoelectronics applications $^{1-3}$. The ability to deterministically create and manipulate charged domain walls is essential to realize their functional properties in electronic devices. Here we report a strategy for the controllable creation and manipulation of in-plane charged domain walls in BiFeO₃ ferroelectric films a few nanometres thick. By using an in situ biasing technique within a scanning transmission electron microscope, an unconventional layer-by-layer switching mechanism is detected in which ferroelectric domain growth occurs in the direction parallel to an applied electric field. Based on atomically resolved electron energy-loss spectroscopy, in situ charge mapping by in-line electron holography and theoretical calculations, we show that oxygen vacancies accumulating at the charged domain walls are responsible for the domain-wall stability and motion. Voltage control of the in-plane domain-wall position within a BiFeO₃ film gives rise to multiple non-volatile resistance states, thus demonstrating the key functional property of being a memristor a few unit cells thick. These results promote a better understanding of ferroelectric switching behaviour and provide a new strategy for creating unit-cell-scale devices.

Ferroelectricity is when materials exhibit a spontaneous electric polarization that is switchable by an applied electric field, which makes it a useful property for various technological applications⁴. As recently as two decades ago, ferroelectricity was commonly considered to be a macroscopic phenomenon and, consequently, ferroelectric materials were sidelined by the nanoscience boom. In the intervening time, the field has seen an extraordinary turnaround. New applications of ferroelectrics down to the nanometre scale have been demonstrated^{1,2}, turning the focus of the field onto low-dimensional geometry. Recent developments have pushed the limits even further, aiming to deterministically control the nanodomains and subnanometre-thick domain walls³, making it possible to manipulate ferroelectric switching at the atomic scale. By engineering the desired properties of domain walls, new findings indicate the possibility of using a single domain wall as an electronic device5.

Ferroelectric domain walls are regions that separate uniformly polarized domains with different polarization orientations. Domain walls exhibit reduced dimensionality and different symmetry from the host material, giving rise to physical properties that do not exist in the surrounding uniformly polarized domains. For example, domain-wall conductivity⁶⁻¹¹ and unconventional magnetic¹² and optical¹³ properties of domain walls have been discovered in ferroelectric thin films such as BiFeO₃(BFO)^{6,11,13}, ErMnO₃(refs. ^{7,10,12}) and BaTiO₃ (refs. ^{8,9}).

Domain walls can be either electrically neutral or charged. The neutral domain walls carry no net bound charge, that is, the normal component of polarization is continuous across the wall. By contrast, in a charged domain wall, bound charges appear at the wall owing to discontinuity of the normal component of polarization. Domain walls can also be out-of-plane or in-plane depending on whether they are perpendicular or parallel to the film surface. In ferroelectric thin films with out-of-plane electric polarization, electrically neutral out-of-plane domain walls normally occur (Fig. 1a), which keep both the domain-wall energy density and the domain-wall area low. The charged in-plane domain walls (Fig. 1b) are much rarer in such ferroelectric films, owing to a large electrostatic energy associated with the polarization charge as well as a large domain-wall area that is not limited by film thickness. Although such domain walls are uncommon, they offer new functionalities that are not provided by the out-of-plane domain walls. A notable

¹Center of Electron Microscopy, School of Materials Science and Engineering, Zhejiang University, Hangzhou, China. ²Department of Materials Science and Engineering, National University of Singapore, Singapore City, Singapore. 3Shenyang National Laboratory for Materials Science, Institute of Metal Research, Chinese Academy of Sciences, Shenyang, China. 4Department of Physics and Astronomy & Nebraska Center for Materials and Nanoscience, University of Nebraska-Lincoln, NE, USA. 5Department of Physics, South Dakota School of Mines and Technology, Rapid City, SD, USA, ⁶Department of Physics, Zhejiang University, Hangzhou, China, ⁷State Key Laboratory of Silicon Materials, School of Materials Science and Engineering, Zhejiang University, Hangzhou, China. 8School of Physics and Microelectronics, Zhengzhou University, Zhengzhou, China. 9These authors contributed equally: Zhongran Liu, Han Wang, Ming Li. [™]e-mail: tsymbal@unl.edu; mseci@nus.edu.sg; zezhang@ziu.edu.cn; hetian@ziu.edu.cn

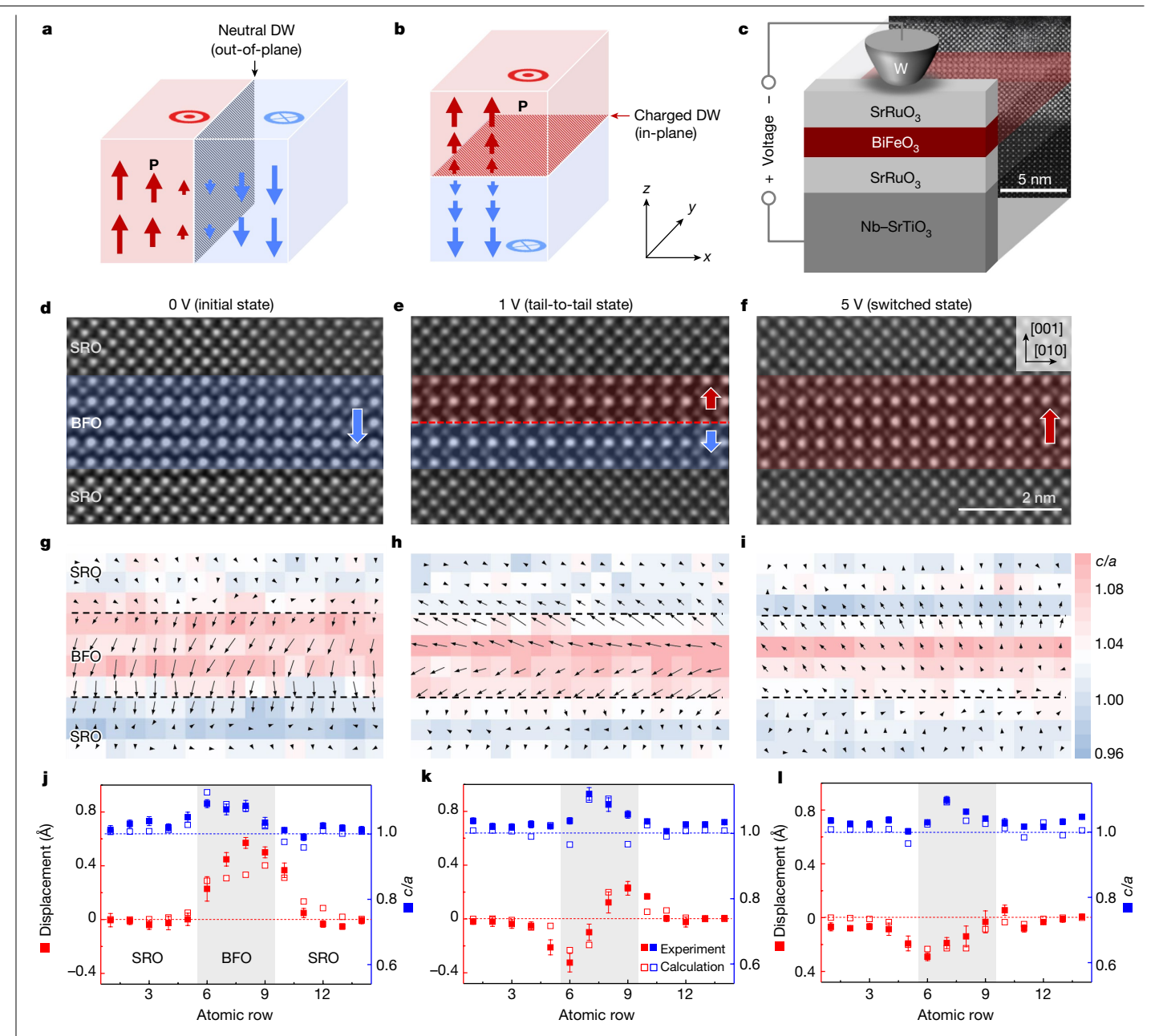


Fig. 1 | Real-time observation of ferroelectric domain switching behaviour. a,b, A neutral out-of-plane (a) and charged in-plane (b) domain wall (DW) in a ferroelectric film with out-of-plane electric polarization. The arrows represent the polarization vectors **P. c**, A sketch of the SRO-BFO-SRO heterostructure and the in situ biasing experiment. d-f, HAADF-STEM images of the SRO-BFO-SRO film cross-section in the (100) plane under an in situ electric bias of 0 V (d), 1 V (e) and 5 V (f). The normal component of polarization in BFO is indicated by red and blue arrows, and the domain wall is marked by a red dashed line in e. \mathbf{g} - \mathbf{i} , The cross-sectional lattice map, in which the c/a ratio is indicated by colour

at each unit cell of the structures displayed in $\mathbf{d} - \mathbf{f}$, respectively, and polarization vectors are indicated by black arrows. j-l, The plane-averaged c/a ratio (solid blue squares) and out-of-plane off-centre displacement (solid red squares) compared with DFT calculations (open blue and red squares, respectively) for the structures displayed in $\mathbf{d} - \mathbf{f}$, respectively. The error bars reflect the standard error of the mean in each atomic row. A positive value of off-centre $displacement\ indicates\ that\ the\ displacement\ is\ along\ the\ [001]\ direction.$ By using the in situ technique, the whole process of domain switching is performed dynamically at the atomic scale.

example is a ferroelectric tunnel junction (FTJ)¹⁴ that exploits switchable polarization of an ultrathin ferroelectric barrier to control tunnelling conductance, in which an in-plane domain wall creates quantum confinement leading to resonant tunnelling¹⁵ and domain-wall tunnelling electroresistance effects¹⁶.

The quasi-two-dimensional nature of domain walls is appealing for nanoelectronics owing to emerging opportunities for the design of electronic building blocks and circuitry at the nanoscale. To realize this potential, the deterministic control of domain walls is essential for device operation. However, previously the manipulation of domain walls has been mostly performed at the micrometre scale^{7-9,17-19}. The control of domain walls, especially charged domain walls, is still lacking at the atomic scale, but it is important in the miniaturization of electronic devices. Such control requires direct monitoring of the polarization reversal process under an applied electric field down to subangstrom spatial resolution, which is technically hugely challenging. The precise monitoring of domain-wall dynamics behaviour and the accompanying charge transfer are essential for explaining the mechanism of polarization reversal, which is critical for creating new thin-film ferroelectric devices.

In this work we report a strategy to create, move and erase an in-plane charged domain wall with a 'tail-to-tail' configuration in SrRuO $_3$ (SRO)–BFO–SRO heterostructures. Layer-by-layer ferroelectric switching is directly observed accompanied by charge accumulation, by using an insitu biasing technique. The whole process of polarization reversal is investigated step by step and atom by atom, by using high-angle annular dark-field scanning transmission electron microscopy (HAADF–STEM) imaging. A combination of electron energy-loss spectroscopy (EELS), in-line holography and first-principles density functional theory (DFT) calculations reveals the motion of a charged domain wall through positively charged oxygen vacancies. By using voltage control of the domain-wall positioning within the BFO film, multiple non-volatile resistance states are realized, demonstrating the key functional property of being a memristor a few unit cells thick.

The designed SRO-BFO-SRO trilayer structure is shown in Fig. 1c. A ferroelectric BFO film of variable thickness, ranging from 2 unit cells to 20 unit cells, is sandwiched between 5-nm-thick symmetric conductive SRO electrodes. The film is grown on a (001) Nb-doped SrTiO $_3$ (STO) single-crystal substrate (Extended Data Fig. 1). An external insitu bias voltage is applied by a tungsten probe (Methods and Extended Data Fig. 2), while atomic HAADF-STEM images of the film are simultaneously recorded (Fig. 1d–f). Both the top and bottom BFO-SRO interfaces are atomically sharp as indicated by the clear contrast. For each unit cell, the c/a lattice parameter ratio and polarization vector are extracted from the STEM images (Methods) and are displayed in Fig. 1g–i. As is evident from Fig. 1j–l, variations of the plane-averaged c/a ratio and the off-centre displacement across the SRO-BFO-SRO trilayer obtained from the STEM data are in excellent agreement with those obtained from our DFT calculations (Methods).

A nanometre-thick BFO film exhibits a single ferroelectric domain structure at the initial state (Fig. 1d,g,j). Polarization vectors have a uniform out-of-plane direction in all BFO atomic layers, showing a high spontaneous polarization consistent with previous work²⁰. However, when an in situ bias of 1 V is applied, an atomically flat in-plane domain wall is created (Fig. 1e,h,k). This domain wall is characterized by the normal components of polarization pointing away from the domain-wall plane, thus representing a charged tail-to-tail domain wall. At the domain-wall area, the lattice structure exhibits a distortion with c/a = 1.08-1.10, largely owing to the changing c parameter across the structure (Extended Data Fig. 3). Surprisingly, the created in-plane charged domain wall is very stable. Even when the bias voltage is turned off, the BFO film still maintains this tail-to-tail polarization over a long time (Extended Data Fig. 4). When the applied in situ voltage rises to 5 V, the charged domain wall vanishes and the polarization is $fully \, reversed \, (Fig. \, 1f, i, l). \, Thus, by \, using \, the \, designed \, heterostructure$ and the in situ biasing technique, a charged domain wall is created and erased in the BFO film plane.

A layer-by-layer motion of the domain wall is observed with applied bias changing from 0.5 to 1.5 V. Figure 2a-c shows the dynamic transformation of the polarization profile across the BFO film with the increasing applied voltage. It is seen that the tail-to-tail domain wall migrates steadily from one BFO atomic layer to another, showing layer-by-layer polarization switching. Because a charged domain wall is expected to be energetically unfavourable, there must be an underlying mechanism for screening the polarization charges at the domain wall. To explain the screening mechanism, we investigated the charge distribution across the domain wall during its migration by using EELS and in-line electron holography techniques complemented by DFT calculations (Methods). Fine structures in the EELS Fe-L and O-K edges are quantified as the Fe/O abundance ratio (right panels of Fig. 2a-c). At the domain-wall area, the Fe/O ratio is notably enhanced. This is because of the reduction in the O concentration at the domain wall as no relative change in the Fe concentration is observed from the EELS data (Extended Data Fig. 5). The Fe/O atomic ratio determined from the EELS data indicates an enhanced population of positively charged

oxygen vacancies at the domain wall, which is also evidenced by the distortions of the oxygen octahedra (Extended Data Fig. 6). This conclusion is confirmed by our DFT calculations, which show that oxygen vacancies in the SRO-BFO-SRO structure help to stabilize the in-plane domain-wall configuration (right panels in Fig. 2d-fand Extended Data Fig. 7). Ionized oxygen vacancies provide a positive bound charge that screens the negative polarization charge at the tail-to-tail domain wall, whereas the negative electron charge goes to the interfaces, resulting in a stable domain-wall configuration. The explicit charge balance across the domain wall is obtained from in-line holography measurements, which allow the direct detection of the charge distribution with high resolution and accuracy²¹⁻²³. Figure 2d-f shows the obtained evolution of the charge distribution with the domain-wall motion from the top to bottom interface. It is seen that a positive charge density is accumulated at an in-plane localized area, precisely where the charged domain wall is.

The motion of the domain wall across the ferroelectric layer is accompanied by changes in the electrical resistance of the SRO-BFO-SRO FTJ (see Methods for the details of I-V measurements), which exhibits distinctive memristive features that are characterized by multiple non-volatile resistance states. The I-V characteristics of the FTJ reveal pinched hysteresis loops (Extended Data Fig. 8a), which is a signature of the memristive behaviour 24,25 . Notably, the measured electric current and the associated resistance display pronounced jumps with increasing voltage. In Fig. 2g-h, three current and resistance jumps are observed. The resistance decreases in a step-like pattern, distinct from the stepless change in ordinary memristors in which a conductive filament is formed and ruptured 26,27 . It is notable that the step-like I-V feature persists in a much larger area of the sample (Extended Data Fig. 8b). These tests demonstrate the non-volatile character of these resistance states, which can be obtained at specific values of voltage.

The observed stepwise character of the resistance originates from the layer-by-layer motion of the ferroelectric domain wall across the BFO film under the applied bias voltage. By measuring the resistance during the in situ biasing process (Extended Data Fig. 8c,d) and simultaneously monitoring the polarization configurations (Fig. 2i,i), clear correlation is found between the resistance steps and the different positions of the domain wall within the BFO layer. This process reveals good reproducibility and reversibility. Therefore, the 'quantized' resistance behaviour is associated with the in-plane domain wall moving layer-by-layer and being stabilized at each atomic layer in BFO for a certain bias voltage. Each of these domain-wall states are characterized by different resistance values between those two associated with the polarization states at saturation. This mechanism is different from resonant tunnelling resulting in conductance steps owing to the quantum-well states associated with a ferroelectric domain wall 15,16. Thus, by applying a voltage, not only is layer-by-layer switching realized, but also multiple polarization and resistance states can be precisely and reversibly controlled. Along with the motion of a charged domain wall, the resistance can be modulated at the unit-cell scale—the minimum scale for multiple resistance-state device control. This property manifests a new type of a unit-cell-level FTJ memristor, which is determined by the voltage-controlled positioning of the in-plane domain wall within the ferroelectric layer, as shown in Fig. 2k. This type of memristor is different from the ferroelectric memristor, in which the fraction of the switched domain determines the FTJ resistance²⁸.

The observed layer-by-layer polarization switching mechanism is characterized by the ferroelectric domain growth in the direction parallel to the applied electric field, which is different from the conventional mechanism in which the ferroelectric domain polarized along the field direction grows perpendicular to the applied field $^{29-31}$. This is due to the polarization and screening charges being distributed uniformly parallel to the BFO film plane, rather than being accumulated at specific nucleation sites 8,32 . This special charge distribution pattern originates from the symmetric SRO-BFO-SRO layered structure design, in which the same atomic termination is engineered at both interfaces with a BiO

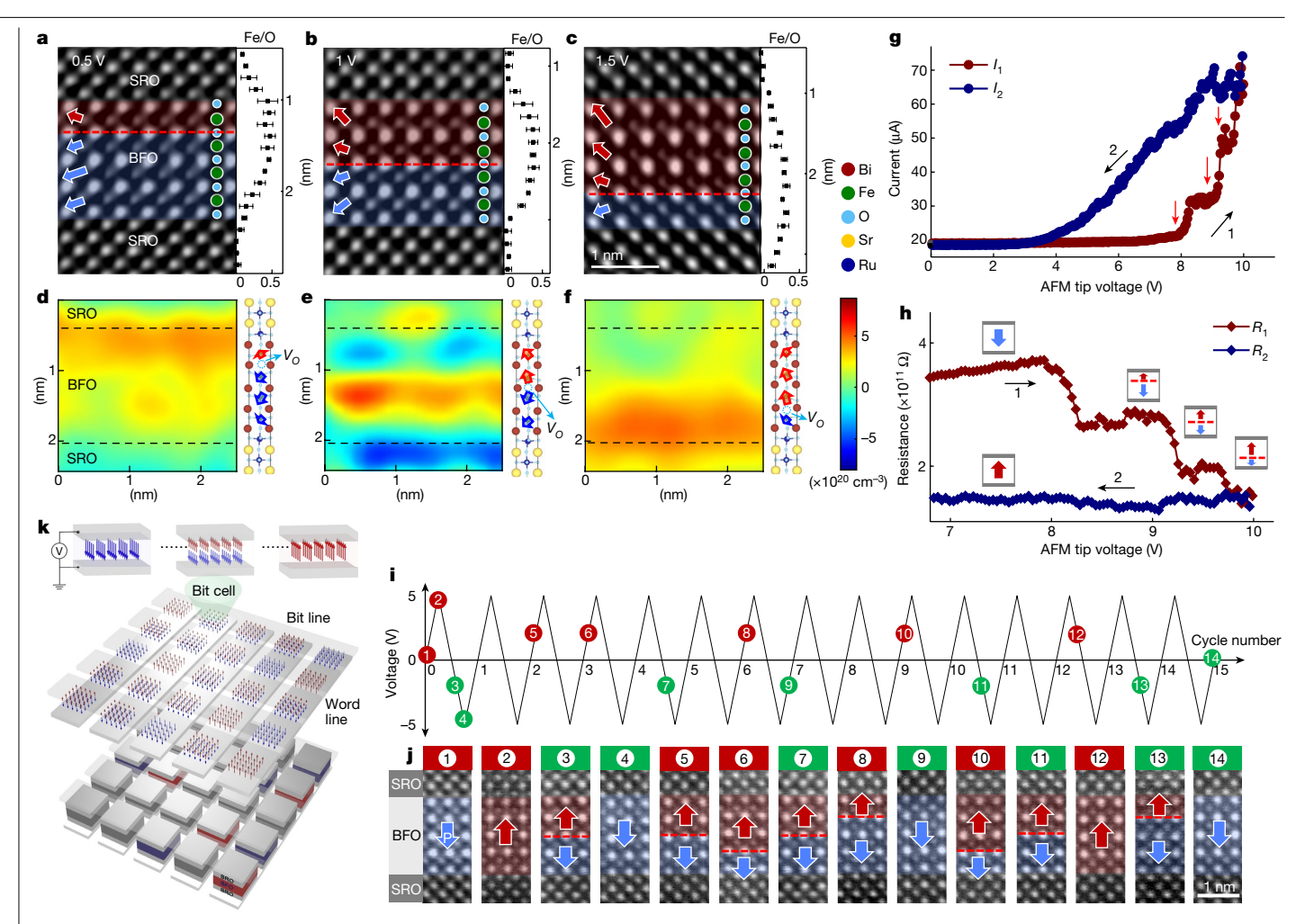


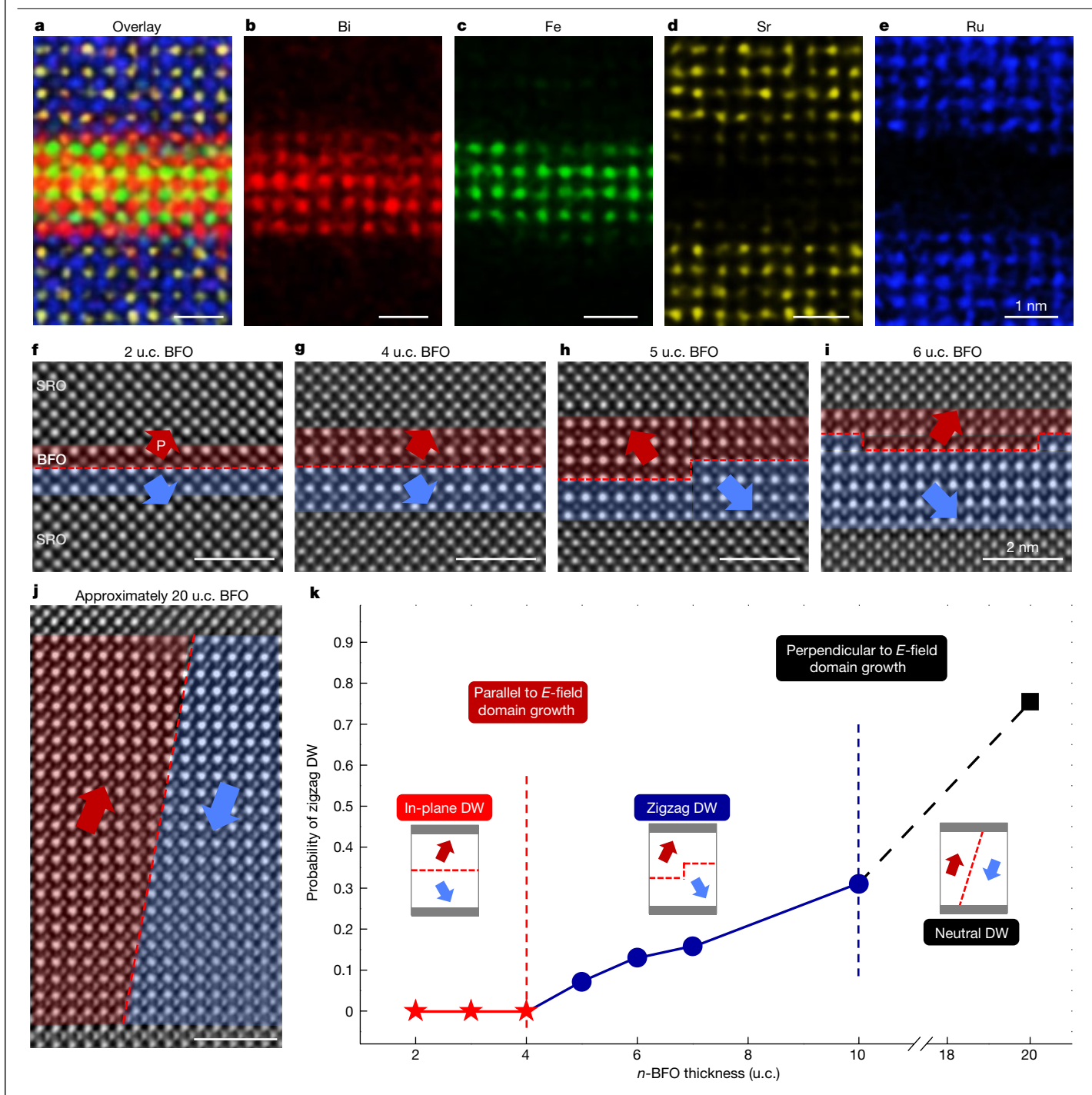
Fig. 2 | Layer-by-layer domain-wall migration with multiple resistance states.a-c, HAADF-STEM images of SRO-BFO-SRO film with controlled voltages of 0.5 V (a), 1 V (b) and 1.5 V (c). The polarization vectors (red and blue arrows) and domain walls (red dashed lines) are superposed. The right panels show the Fe/O abundance ratio obtained from EELS across the BFO structures. The error bars are the standard errors for determining the quantification ratio over five EELS line-scanning measurements. **d**-**f**, Charge distribution mapping of the polarization states in $\mathbf{a} - \mathbf{c}$, respectively. The SRO-BFO interfaces are indicated by black dashed lines. The right panels show the results of the DFT calculations for the SRO-BFO-SRO heterostructures with oxygen vacancies $(V_0$, blue circles) at the domain walls. The block arrows indicate the polarization vectors. \mathbf{g} , \mathbf{h} , The I-V curves (\mathbf{g}) and the corresponding R-V curves (\mathbf{h}) resulting

from layer-by-layer polarization switching. The black arrows show the sweeping direction of the voltage. The red arrows in **g** indicate current jumps as the voltage increases (wine-coloured line). The abrupt resistance shifts in **h** follow the layer-by-layer domain-wall motion, resulting in distinct polarization states with the domain wall located at different atomic layers of BFO (insets). i,j, The reversibility of the charged domain-wall motion. The polarization state of BFO shown in j corresponds to the checkpoints in the voltage cycling shown in i with red (green) points indicating positive (negative) voltages. k. Schematic of an envisioned memory crossbar array based on the SRO-BFO-SRO heterostructure with multiple polarization states as bit cells. The polarization charges are accumulated at tail-to-tail domain walls and move layer-by-layer in BFO film forming multiple resistance levels.

monolayer in BFO facing a RuO₂ monolayer in SRO. This termination is evident from the SRO-BFO-SRO atomic structure obtained from our elemental energy-dispersive X-ray (EDX) spectroscopy measurements (Fig. 3a-e). The symmetric interface structure is not prone to producing a built-in electric field across the ferroelectric spacer layer and, thus, when the ferroelectric layer is thin enough, it is capable of sustaining the charged domain wall with the associated screening charges. On the contrary, for the similar SRO-BFO-SRO structure with asymmetric interfaces, the layer-by-layer polarization switching mechanism is extinguished by the presence of a built-in field across the BFO layer (Extended Data Fig. 9). As a result, in symmetrically terminated SRO-BFO-SRO structures with a thin BFO layer of several unit cells, the domain wall is widely observed to be atomically flat without nucleation steps (Fig. 3f,g). However, with an increase of BFO thickness, screening by oxygen vacancies becomes less homogeneous, resulting in an increased probability of obtaining a domain wall with a nucleation feature (Fig. 3h, i and Extended Data Fig. 10). Domain walls start to

zigzag, and eventually become charge-neutral out-of-plane walls in a bulk-like 20-unit-cell-thick BFO film (Fig. 3j). As a result, the ferroelectric polarization switching mechanism changes from the layer-by-layer motion parallel to the applied electric field (E-field) to conventional ferroelectric domain growth perpendicular to the applied field (Fig. 3k). Based on these observations, the necessary conditions to stabilize an in-plane domain wall in a ferroelectric film and to realize layer-by-layer polarization switching are symmetric interfaces of the ferroelectric layer, their in-plane homogeneity on the atomic scale and sufficiently small thickness of the ferroelectric layer.

Our direct observation of in-plane charged domain walls in ferroelectric heterostructures designed to be a few nanometres thick, their deterministic creation, manipulation and annihilation by applied voltage, as well the demonstration of their memristive functionality associated with the multiple non-volatile resistance states, have important consequences both for the fundamental understanding of the domain-wall properties in nanoscale ferroelectrics and for their



are separated by domain walls (red dashed lines). Scale bars, 2 nm. **k**, A diagram of the domain growth and domain-wall type under varying BFO film thickness (n-BFO). The probability of a zigzag domain wall (DW) is calculated by $N_{\rm OP}/(N_{\rm IP}+N_{\rm OP})$ with $N_{\rm OP}$ and $N_{\rm IP}$ being the number of unit cells along the out-of-plane and in-plane directions, respectively.

application in advanced technologies. In particular, the unambiguous correlation between the charged defects (oxygen vacancies) and the domain-wall stability and motion puts forward the importance of electrochemistry in the observed ferroelectric phenomena at the nanoscale³³. The high mobility of oxygen vacancies and their ability to efficiently screen polarization charges may control the ferroelectric switching behaviour in various types of FTJs^{34,35} as well as in bulk ferroelectrics, such as the recently discovered orthorhombic hafnia^{36,37}. Clearly, the discovered mechanism of in-plane domain-wall formation

and layer-by-layer polarization switching has general importance and may occur in ferroelectric capacitors and FTJs with different types of metal electrodes and ferroelectric spacer materials, such as $La_{0.7}Sr_{0.3}MnO_3$ –BFO– $La_{0.7}Sr_{0.3}MnO_3$ and SRO–BaTiO $_3$ –SRO (Extended Data Fig. 11). The in-plane domain wall may be considered to be a new interface artificially created within the ferroelectric layer, which can be controlled by applied voltage and has dynamic characteristics allowing the real-time adjustment of its position. Owing to electronic confinement and the specific chemical environment, the spatially mobile

ferroelectric domain walls offer a wide range of functional properties such as the demonstrated memristive functionality, which may be useful for new nanoscale ferroelectric devices.

Online content

Any methods, additional references, Nature Portfolio reporting summaries, source data, extended data, supplementary information, acknowledgements, peer review information; details of author contributions and competing interests; and statements of data and code availability are available at https://doi.org/10.1038/s41586-022-05503-5.

- Catalan, G., Seidel, J., Ramesh, R. & Scott, J. F. Domain wall nanoelectronics. Rev. Mod. Phys 84 119-156 (2012)
- 2. Martin, L. W. & Rappe, A. M. Thin-film ferroelectric materials and their applications, Nat. Rev. Mater. 2. 1-14 (2016).
- Sharma, P., Schoenherr, P. & Seidel, J. Functional ferroic domain walls for nanoelectronics. Materials 12, 2927 (2019).
- Scott, J. F. Applications of modern ferroelectrics. Science 315, 954-959 (2007).
- Meier, D. & Selbach, S. M. Ferroelectric domain walls for nanotechnology. Nat. Rev. Mater. 7. 157-173 (2021)
- Seidel, J. et al. Conduction at domain walls in oxide multiferroics. Nat. Mater. 8, 229-234 (2009)
- Meier, D. et al. Anisotropic conductance at improper ferroelectric domain walls. Nat. Mater. 11, 284-288 (2012).
- Sluka, T., Tagantsev, A. K., Bednyakov, P. & Setter, N. Free-electron gas at charged domain walls in insulating BaTiO₃. Nat. Commun. 4, 1808 (2013).
- Crassous, A., Sluka, T., Tagantsev, A. K. & Setter, N. Polarization charge as a reconfigurable quasi-dopant in ferroelectric thin films. Nat. Nanotechnol. 10, 614-618 (2015).
- Mundy, J. A. et al. Functional electronic inversion layers at ferroelectric domain walls. Nat. Mater. 16, 622-627 (2017).
- Rojac, T. et al. Domain-wall conduction in ferroelectric BiFeO₃ controlled by accumulation of charged defects, Nat. Mater. 16, 322-327 (2017).
- Geng, Y, et al. Direct visualization of magnetoelectric domains, Nat. Mater. 13, 163-167 (2014).
- 13. Yang, S. Y. et al. Above-bandgap voltages from ferroelectric photovoltaic devices. Nat. Nanotechnol 5 143-147 (2010)
- Tsymbal, E. Y. & Kohlstedt, H. Tunneling across a ferroelectric. Science 313, 181-183
- 15. Sanchez-Santolino, G. et al. Resonant electron tunnelling assisted by charged domain walls in multiferroic tunnel junctions. Nat. Nanotechnol. 12, 655-662 (2017).
- Li, M., Tao, L. L. & Tsymbal, E. Y. Domain-wall tunneling electroresistance ffect. *Phys. Rev.* Lett. 123, 266602 (2019).
- McGilly, L. J., Yudin, P., Feigl, L., Tagantsev, A. K. & Setter, N. Controlling domain wall motion in ferroelectric thin films. Nat. Nanotechnol. 10, 145-150 (2015).

- Gao, P. et al. Direct observations of retention failure in ferroelectric memories, Adv. Mater. 24, 1106-1110 (2012).
- Jiang, J. et al. Temporary formation of highly conducting domain walls for non-destructive read-out of ferroelectric domain-wall resistance switching memories. Nat. Mater. 17, 49-56
- Wang, H. et al. Direct observation of room-temperature out-of-plane ferroelectricity and tunneling electroresistance at the two-dimensional limit. Nat. Commun. 9, 3319 (2018).
- Lee, H. et al. Direct observation of a two-dimensional hole gas at oxide interfaces, Nat. Mater. 17, 231-236 (2018).
- Song, K. et al. Direct imaging of the electron liquid at oxide interfaces. Nat. Nanotechnol. 13, 198-203 (2018).
- Liu, S. et al. Towards quantitative mapping of the charge distribution along a nanowire by in-line electron holography. Ultramicroscopy 194, 126-132 (2018).
- 24. Chua, L. If it's pinched it's a memristor, Semicond, Sci. Technol. 29, 104001 (2014).
- Ouaia Rziga, F., Mbarek, K., Ghedira, S. & Besbes, K. The basic I-V characteristics of memristor model: simulation and analysis, Appl. Phys. A 123, 288 (2017).
- 26. Yang, J. J., Strukov, D. B. & Stewart, D. R. Memristive devices for computing, Nat. Nanotechnol, 8, 13-24 (2013).
- Lian, X, et al. Characteristics and transport mechanisms of triple switching regimes of TaOx memristor, Appl. Phys. Lett. 110, 173504 (2017).
- 28 Chanthboulala A et al. A ferroelectric memristor. Nat. Mater. 11, 860–864 (2012).
- Shin, Y. H., Grinberg, I., Chen, I. W. & Rappe, A. M. Nucleation and growth mechanism of ferroelectric domain-wall motion. Nature 449, 881-884 (2007).
- 30. Nelson, C. T. et al. Domain dynamics during ferroelectric switching. Science 334, 968-971 (2011)
- Liu, S., Grinberg, I. & Rappe, A. M. Intrinsic ferroelectric switching from first principles. Nature 534, 360-363 (2016).
- Rodriguez, B. J. et al. Unraveling deterministic mesoscopic polarization switching mechanisms: spatially resolved studies of a tilt grain boundary in bismuth ferrite. Adv. Funct. Mater. 19, 2053-2063 (2009).
- Kalinin, S. V. & Spaldin, N. A. Functional ion defects in transition metal oxides. Science 341, 858-859 (2013).
- 34. Kim, D. J. et al. Ferroelectric tunnel memristor. Nano Lett. 12, 5697-5702 (2012).
- Hernandez-Martin, D. et al. Controlled sign reversal of electroresistance in oxide tunnel junctions by electrochemical-ferroelectric coupling. Phys. Rev. Lett. 125, 266802 (2020).
- Nukala, P. et al. Reversible oxygen migration and phase transitions in hafnia-based ferroelectric devices. Science 372, 630-635 (2021).
- 37. Yun, Y. et al. Intrinsic ferroelectricity in Y-doped HfO₂ films, Nat. Mater. 21, 903-909 (2022).

Publisher's note Springer Nature remains neutral with regard to jurisdictional claims in published maps and institutional affiliations.

Springer Nature or its licensor (e.g., a society or other partner) holds exclusive rights to this article under a publishing agreement with the author(s) or other rightsholder(s): author self-archiving of the accepted manuscript version of this article is solely governed by the terms of such publishing agreement and applicable law.

© The Author(s), under exclusive licence to Springer Nature Limited 2023

Methods

Sample preparation

The SRO-BFO-SRO trilayer structures with different thicknesses were grown by a laser-molecular beam epitaxy technique onto atomically smooth (001) Nb-doped (0.7 wt%) STO single-crystal substrates (Crystec GmbH) with a small miscut angle (<0.5°) by using a KrF (wavelength 248 nm) laser. Here the conducting SRO layers were used as the top and bottom electrodes. A laser spot size of 4 mm² at a frequency of 3 Hz was created for ablating the stoichiometric targets (Bi_{0.9}FeO₃ and SRO). The substrate was placed at a 6.5 cm distance directly above the BFO and SRO targets. The SRO layers were deposited at a substrate temperature of 600 °C in a flowing oxygen atmosphere of 100 mTorr by using a laser fluence of 1.2 I cm⁻². The conditions for the BFO layer were adjusted to 600 °C and 130 mTorr by using a laser fluence of 1 J cm⁻². During the growth, in situ high-pressure reflective high-energy electron diffraction was used to monitor the film thickness. After deposition, the samples were cooled to room temperature under pure oxygen at a cooling rate of 5 °C min⁻¹ to reduce the oxygen vacancy.

In situ experiment and imaging

Samples were prepared into the cross-sectional lamella by a focused ion beam and were mounted on a Hysitron PI-95 sample holder. A bias voltage was applied by the sample holder, which electrically connected the bottom SRO electrode and the Nb-doped STO conductive substrate (Supplementary Fig. 2). The conductive probe provided an electrical path through the capping Pt and the top SRO layer. A partition was made in the sample to make sure that there was no series connection between the top SRO and the substrate. The microstructure and element distribution were characterized by using aberration-corrected STEM at high-angle annular dark-field mode on an FEI Titan $G^280-200$ microscope at an emission voltage of $200\,\mathrm{kV}$, equipped with a Super-X EDX and Gatan Image Filter (GIF) detector. To reduce random noise in the HAADF-STEM images, a Fourier filter mask was used.

Obtaining cross-sectional lattice parameters map and polarization vectors

The out-of-plane lattice parameters c and the in-plane lattice parameters a were quantified for each unit cell of the structure based on HAADF–STEM measurements. Then a c/a ratio was obtained for each unit cell to characterize the local distortion of the lattice structure. Polarization vectors were obtained from the off-centre displacement of the B-site atom (Fe and Ru) with respect to the A-site atom (Bi and Sr) for each unit cell.

Determination of atomic positions

All atomic column positions in the measurement of off-centre displacements were determined by using a multiple-ellipse fitting method³⁸. Atomic columns were fitted by a series of ellipses to outline the shape and intensity, then were then precisely located.

Theoretical modelling

DFT-based calculations were performed by using the projector-augmented wave method 39,40 , as implemented in the Vienna ab-initio simulation package 41 . An energy cut-off of 400 eV, and an exchange and correlation functional of the local density approximation with Hubbard-U correction (U = 3.5 eV for the Fe-d orbital) were used throughout. The SRO-BFO heterostructure was modelled by a [SRO]_{5.5}-[BFO]_{4.5}-[SRO]₅ superlattice. The in-plane lattice constant was constrained to be the local density approximation calculated value of bulk cubic STO, a = 3.86 Å, to simulate epitaxial growth on a STO substrate. Both SRO and BFO were assumed to be in the tetragonal phase with c/a = 1.01 for bulk SRO and c/a = 1.09 for bulk BFO. The spin-polarized calculations were performed to account for the ferromagnetic state of SRO and the antiferromagnetic state of BFO. For the single domain

structure, the polarization was along the [001] direction characterized by the atomic displacements along the *z* direction. For the tail-to-tail domain-wall structure, the polarization was canted from the [001] direction with a finite [110] polarization component. The oxygen vacancies were modelled by removing one O atom from the central BiO plane. Both the out-of-plane lattice constant and the internal atomic positions were fully relaxed until forces were less than 0.01 eV Å $^{-1}$. A 6 × 6 × 1 (10 × 10 × 1) *k*-point mesh was used for the structural relaxation (self-consistent) calculations.

In-line electron holography measurements

In-line holography was carried out by using TEM (Titan G2 60-300, FEI) operated at 300 kV with an objective aperture of 10 μ m in diameter to select the transmitted beam. A total of 20 bright-field TEM images at defocus values ranging from –1 μ m to +1 μ m were acquired in 100 nm steps. To minimize the electron-beam damage, the bright-field TEM images were obtained at a magnification of 4.9 \times 10 5 under an electron-dose rate of 80 e Å 2 s $^{-1}$. The obtained in-line electron holograms were used to reconstruct the phase shift of the transmitted beam by using iterative methodology $^{21-23}$.

Electrical measurements

The *I*–*V* curve measurements were performed at room temperature by using a commercial atomic force microscope with a conductive-atomic force microscopy (AFM) mode (PARK NX10). The samples were mounted on a round metal holder by using silver paste and were connected to the internal source electrode of the atomic force microscope. Bias sweeps were applied to the sample from the internal source and the current was measured through commercial silicon tips coated with Pt (Multi75E-G, Budget Sensors) by the internal lock-in units of the atomic force microscope. The bias sweeps were settled as a positive to negative voltage circle, like 0 V to +10 V to -10 V to 0 V, with a time period of $100 \text{ s} (0.1 \text{ V s}^{-1})$ and the currents were measured with a limit of 100 µA.

AFM and piezoelectric force microscopy characterizations

The topography and ferroelectricity were measured by using the AFM and piezoelectric force microscopy modes, respectively, of a commercial scanning probe microscope (Asylum Research MFP-3D) at room temperature. For the piezoelectric force microscopy measurements, Pt coated probes (AC240TM, spring constant of approximately 2 N m $^{-1}$, Olympus, Japan) were used under the drive frequency of approximately 270 kHz, a drive amplitude of 1 V and a trigger force of 80 nN (Extended Data Fig. 12).

Data availability

The data generated and analysed during the current study are available from the corresponding authors on reasonable request.

- Zhang, Q. et al. Multiple-ellipse fitting method to precisely measure the positions of atomic columns in a transmission electron microscope image. Micron 113, 99–104 (2018).
- PE, B. Projector augmented-wave method. Phys. Rev. B Condens. Matter 50, 17953–17979 (1994).
- Kresse, G. & Joubert, D. From ultrasoft pseudopotentials to the projector augmentedwave method. *Phys. Rev. B* 59, 1758–1775 (1999).
- Kresse, G. & Furthmüller, J. Efficient iterative schemes for ab initio total-energy calculations using a plane-waye basis set. Phys. Rev. B 54, 11169–11186 (1996).
- Park, T.-J. et al. Electronic structure and chemistry of iron-based metal oxide nanostructured materials: a NEXAFS investigation of BiFeO₃, Bi₂Fe₄O₉, α-Fe₂O₃, γ-Fe₂O₃, and Fe/Fe₃O₄.
 J. Phys. Chem. C 112, 10359–10369 (2008).
- Lazic, I., Bosch, E. G. T. & Lazar, S. Phase contrast STEM for thin samples: integrated differential phase contrast. *Ultramicroscopy* 160, 265–280 (2016).
- Aschauer, U., Pfenninger, R., Selbach, S. M., Grande, T. & Spaldin, N. A. Strain-controlled oxygen vacancy formation and ordering in CaMnO₃. Phys. Rev. B 88, 054111 (2013).
- Gong, J. J. et al. Interactions of charged domain walls and oxygen vacancies in BaTiO₃: a first-principles study. *Mater. Today Phys.* 6, 9–21 (2018).

Acknowledgements We thank G. V. Tendeloo, S. Liu and F. Lin for helpful suggestions regarding revisions to our manuscript. This work was financially supported by the National Key R&D Programme of China (grant no. 2021YFA1500800), the National Natural Science

Foundation of China (grant no. 12125407 and no. 52272129), China Postdoctoral Science Foundation (grant no. 2022M722716), Joint Funds of the National Natural Science Foundation of China (grant no. U21A2067), the Fundamental Research Funds for the Central Universities and the Zhejiang Provincial Natural Science Foundation (grant no. LD21E020002 and no. LR21E020004). J.S.C. acknowledges the financial support from the Singapore Ministry of Education MOET2EP50121-0024, MOE Tier 1-22-4888-A0001, A*STAR AMRIRG (grant no. A1983c0036); RIE2020 Advanced Manufacturing and Engineering (AME) Programmatic Grant no. A20G9b0135; and the Singapore National Research Foundation under a CRP Award (grant no. NRF-CRP23-2019-0070). The research work at the University of Nebraska-Lincoln was supported by the National Science Foundation (NSF) through the EPSCoR RII Track-1 (NSF Award OIA-2044049) and MRSEC (NSF Award DMR-1420645) programmes.

Author contributions Z.Z. and H.T. conceived and designed this work. Z.L. performed and analysed the in situ STEM, EDX and EELS experiments, analysed the electrical measurements and wrote the manuscript. H.W. and J.C. prepared the samples and performed the

characterization. M.L., L.T., T.R.P. and E.Y.T. performed the DFT calculations and data interpretation. H.Y. and Y.W. performed the in-line electron holography measurements. S.H., M.Z. and Y.X. carried out the electrical measurements. Z.R. co-wrote the manuscript. All authors contributed to the manuscript and the interpretation of the data.

Competing interests The authors declare no competing interests.

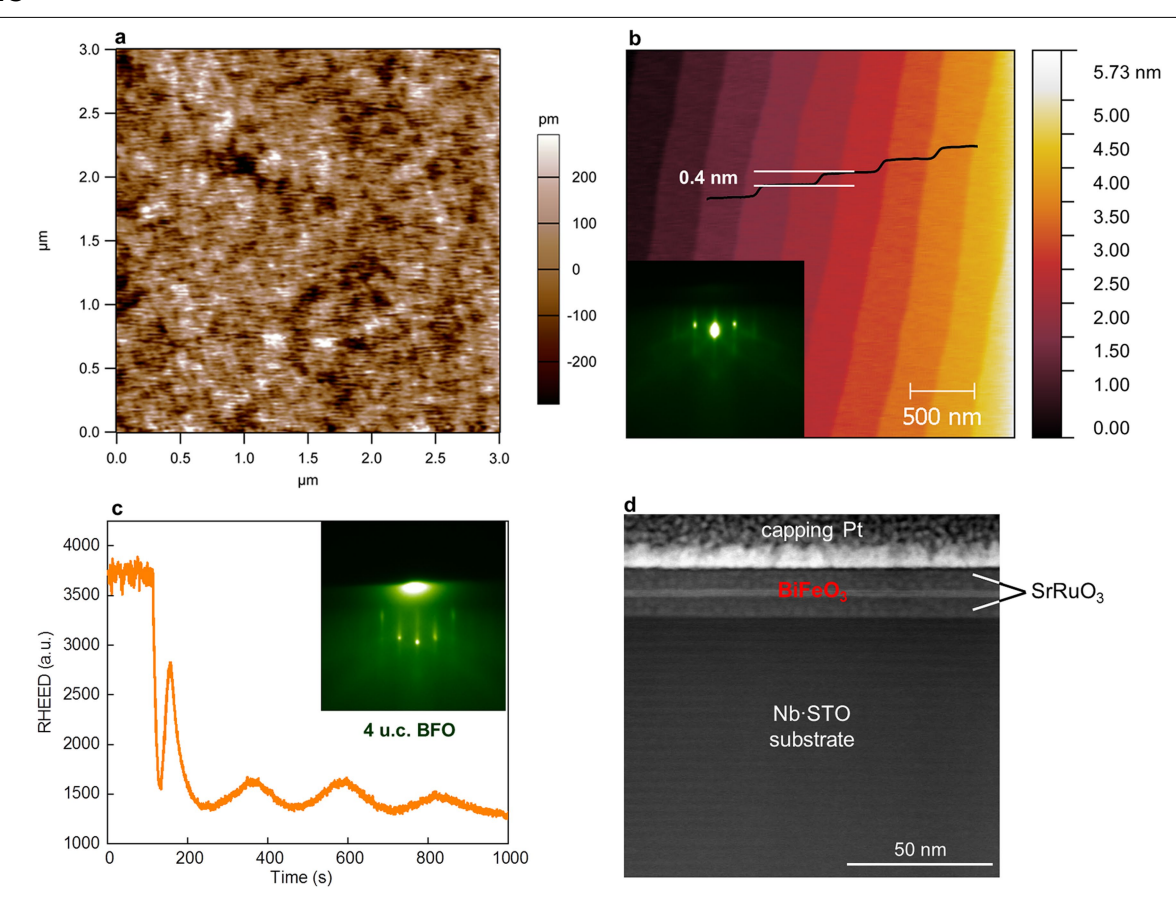
Additional information

Supplementary information The online version contains supplementary material available at https://doi.org/10.1038/s41586-022-05503-5.

Correspondence and requests for materials should be addressed to Evgeny Y. Tsymbal, Jingsheng Chen, Ze Zhang or He Tian.

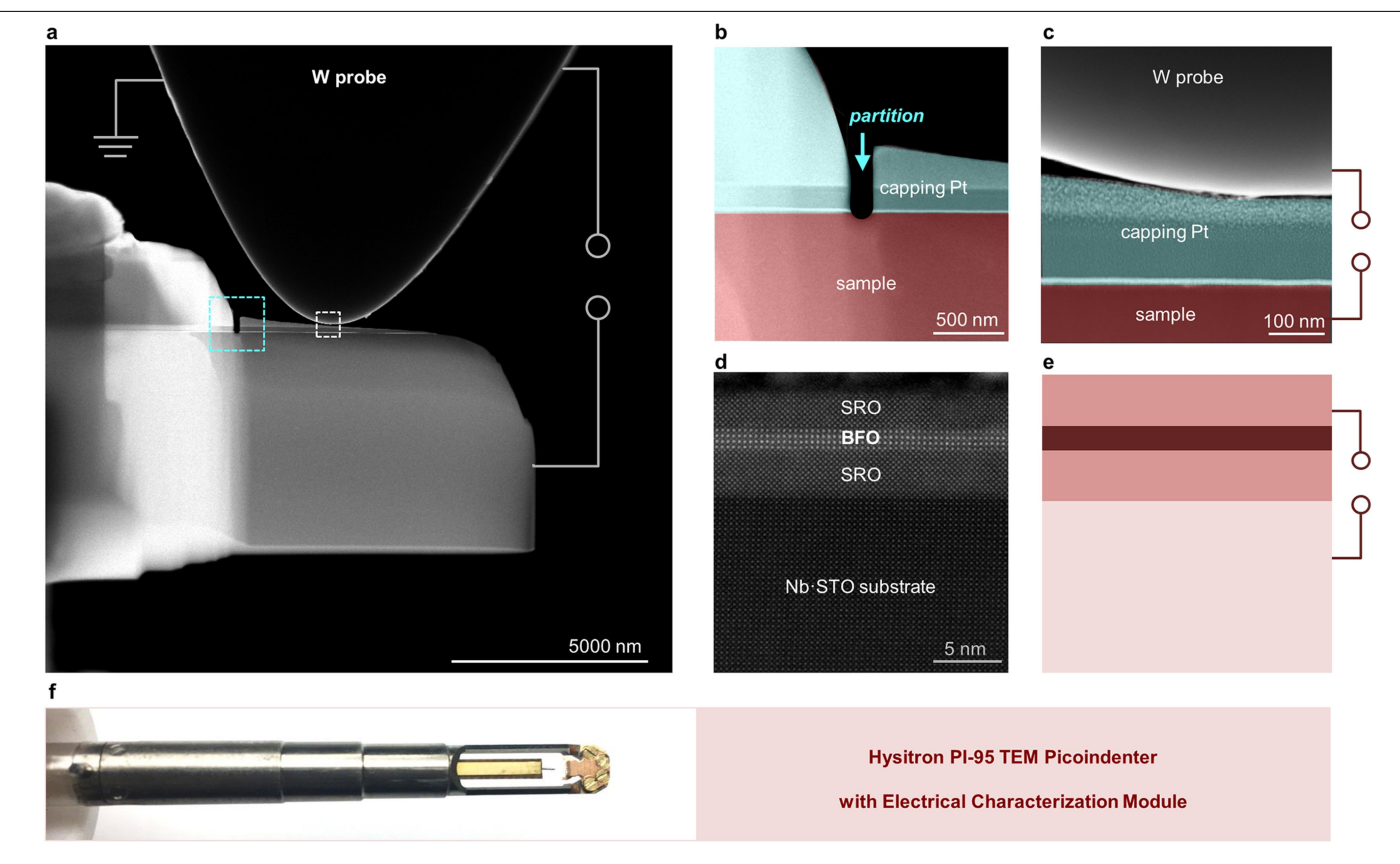
Peer review information *Nature* thanks the anonymous reviewers for their contribution to the peer review of this work. Peer reviewer reports are available.

Reprints and permissions information is available at http://www.nature.com/reprints.



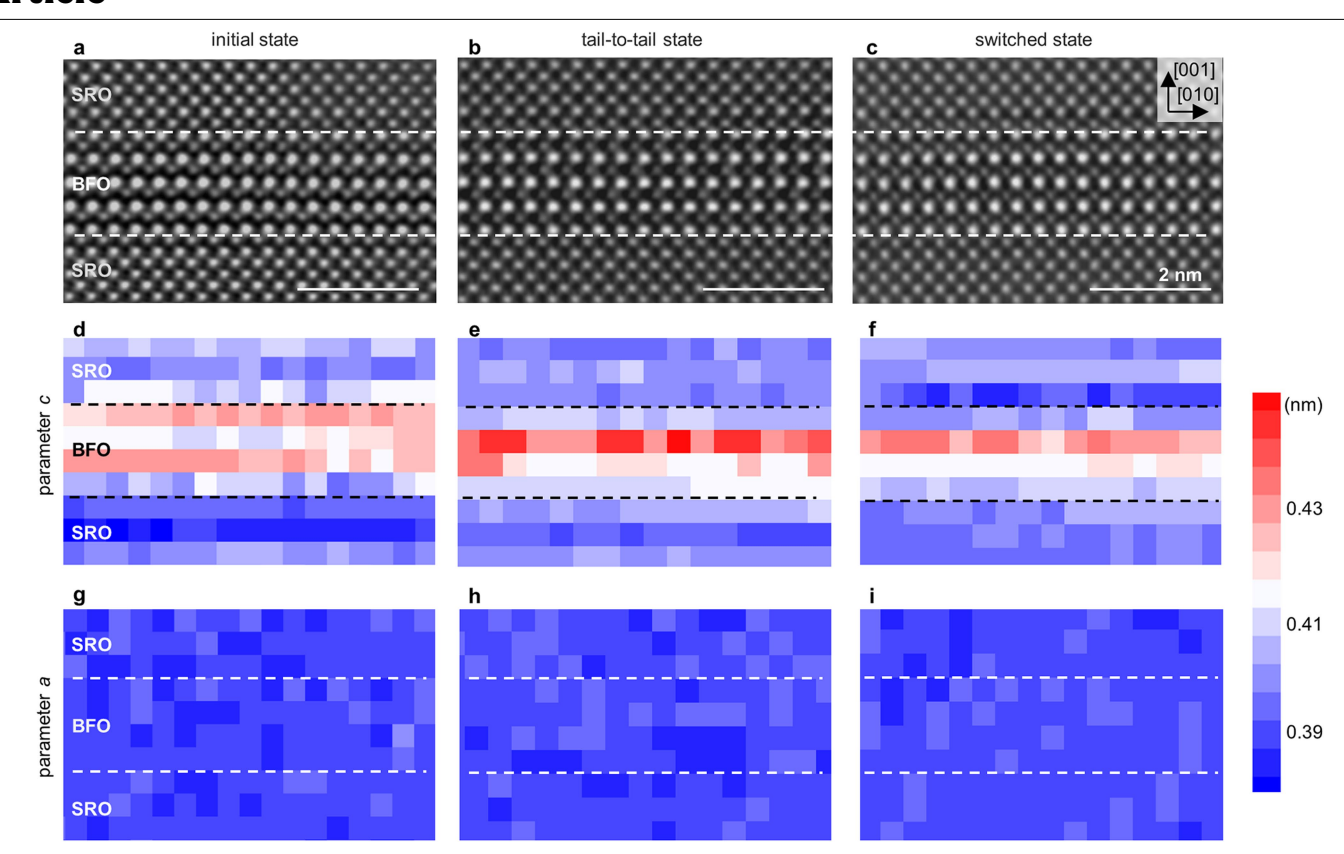
Extended Data Fig. 1 | **Growth of BFO ultrathin films. a**, AFM image of Nb·STO/SRO/BFO/SRO. **b**, AFM images of the morphology of (001) STO substrate. **c**, RHEED intensity oscillation during the growth of SRO and four

unit cell BFO. Insets of (\mathbf{b}, \mathbf{c}) show RHEED patterns of the substrate before and after SRO and BFO deposition respectively. \mathbf{d} , Magnified STEM image of Nb·STO/SRO/BFO/SRO.



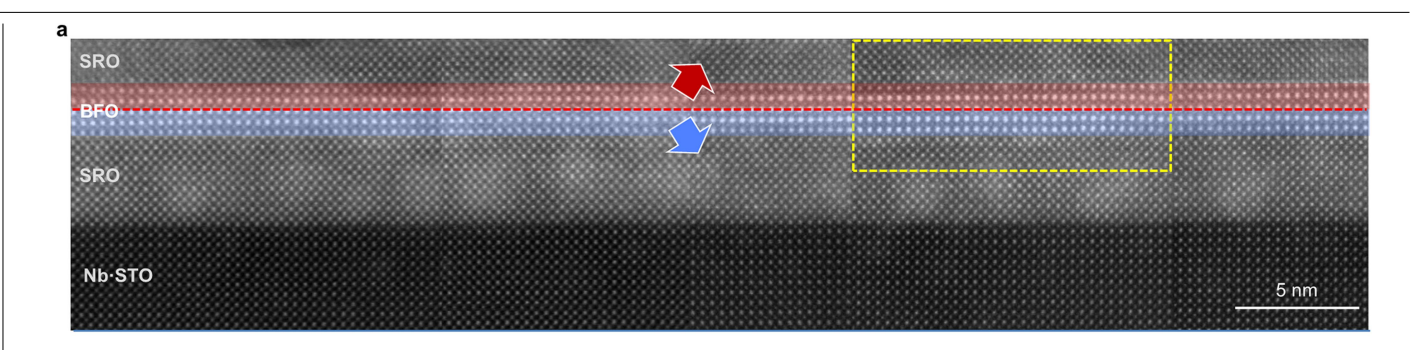
Extended Data Fig. 2 | *In-situ* STEM experiments. a, STEM image of conductive tungsten probe and of FIB sample lamella. The electrical path is marked with white lines. b, Magnified STEM image of partition area highlighted with a dashed blue square in (a). Capping Pt (blue) and sample (red) are cut out until the partition touches the substrate. c, Magnified STEM image of the tip with a

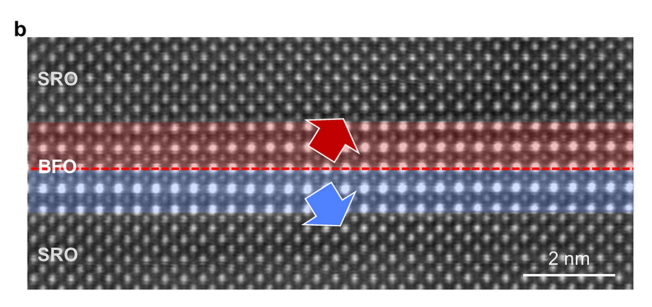
schematic electrical path (red lines), which highlighted by a white square in (a). **d**, Magnified STEM image of SRO/BFO/SRO structure. **e**, Related schematic diagram of (**d**). **f**, Photograph of Hysitron PI-95 TEM Picoindenter with Electrical Characterization Module (ECM).



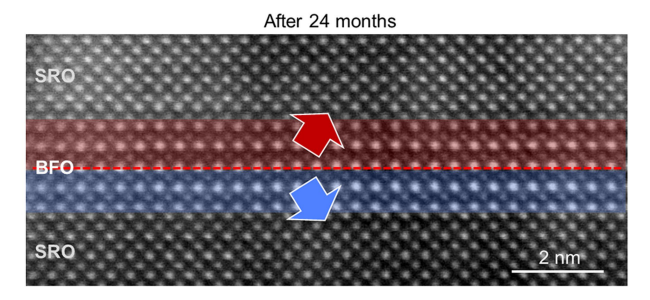
 $\label{lem:extended} \textbf{Extended Data Fig. 3} \ | \ \textbf{Changing of individual lattice parameter c} \ \textbf{a} \ \textbf{during domain switching. a-c}, \ \textbf{HAADF-STEM images of SRO/BFO/SRO} \ which are the same as Fig. 1d-f during polarization switching. Scale bars, 2 nm.$

 \mathbf{d} - \mathbf{f} , Maps of c lattice parameter in $(\mathbf{a}$ - $\mathbf{c})$. \mathbf{g} - \mathbf{i} , Maps of a lattice parameter in $(\mathbf{a}$ - $\mathbf{c})$. To avoid the drift in sample recording, the images are obtained using various beam scanning directions.

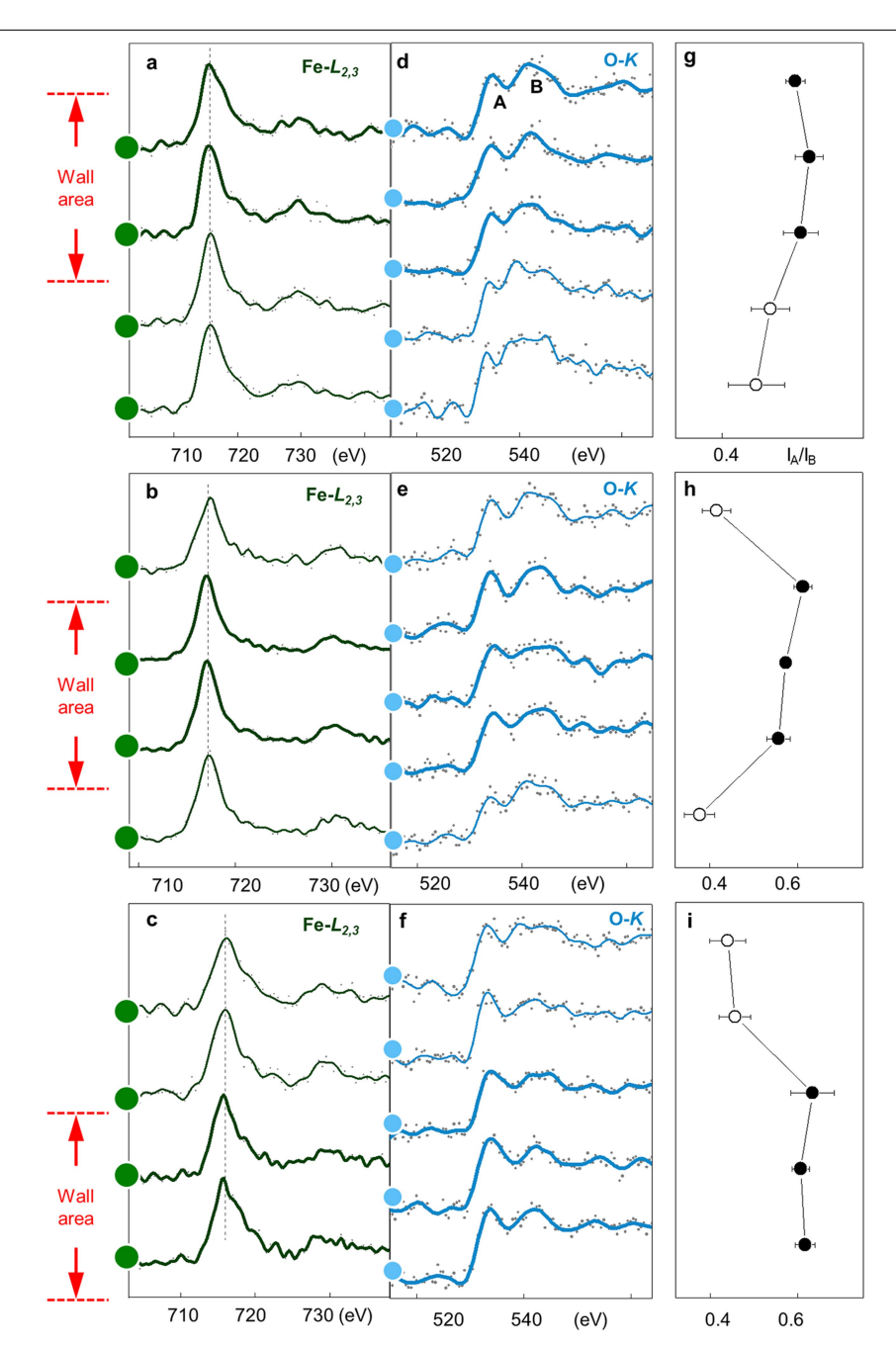




 $\label{lem:extended} \textbf{Data Fig. 4} \ | \textbf{Exhibition of BFO film with tail-to-tail domain wall on large scale and in long time. a}, \textbf{The HAADF-STEM image of BFO film with atomically flat charged domain wall on a large scale. Scale bars, 5 nm. b}, \textbf{The}$

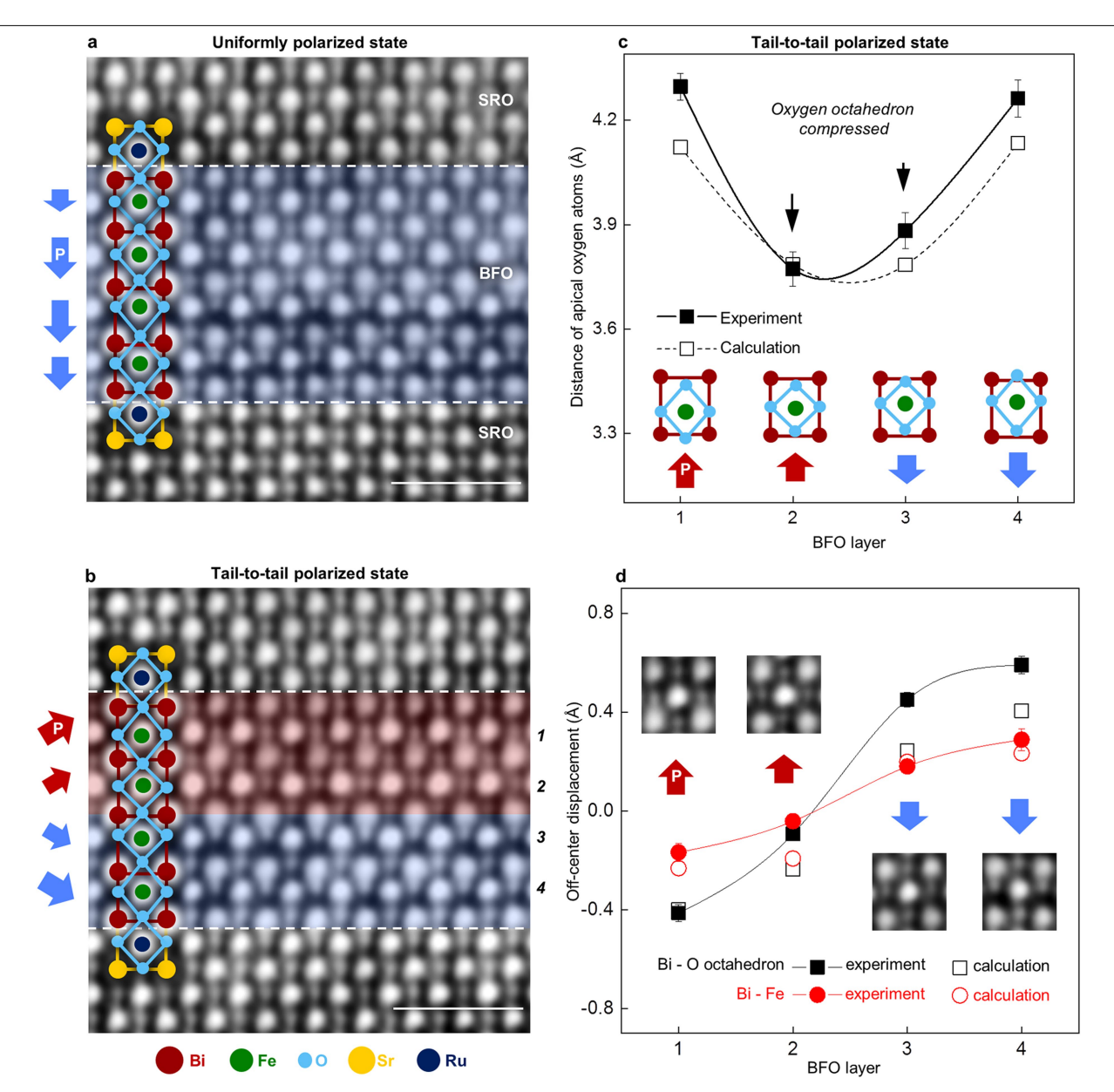


charged domain wall in BFO film after 24 months. The area is highlighted by a yellow rectangle in (a). Tail-to-tail state still maintained for over 24 months. Scale bars, 2 nm.



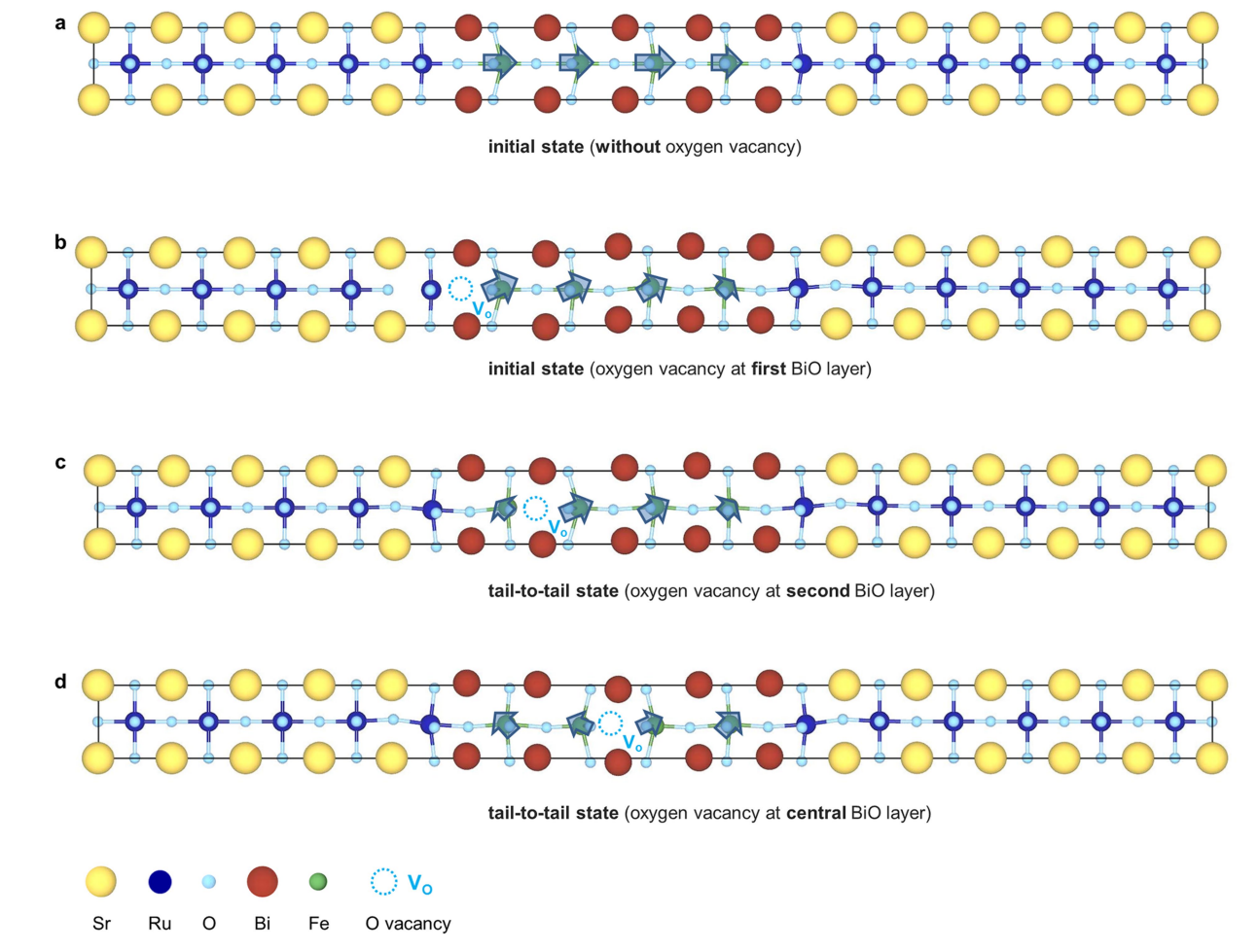
Extended Data Fig. 5 | EELS analysis of Fe-L and O-K edges in different tail-to-tail domain wall states. a-c, Atomic resolution line scanning EELS of Fe- $L_{2,3}$ edges taken along BFO film in Fig. 2a-c. Each spectrum is demonstrated from the signal summing up of one layer of Fe. The shifts of Fe-L edges are less than 0.2 eV, reflecting the unchanged valence state in Fe. **d-f**, Atomic resolution line scanning EELS of O-K edges taken along BFO unit cells in Fig. 2a-c. Original signals are drawn by grey dots, superposed by smoothed spectra. **g-i**, The intensity ratio of peak A and peak B for O-K edges in (**d-f**). The ratio is calculated as $\mathbf{1}_A/\mathbf{1}_B$, indicated by black circles (filled circles: domain wall regions). Error bars

are the standard error for determining the I_A/I_B over five measurements. Two features can be found in the O-K spectra: the pre-peak A, and the post-peak B. The relative intensity of peak A (I_A) and peak B (I_B), displayed as I_A/I_B , is used to evaluate the oxygen vacancy population⁴². In our case, an increased I_A/I_B corresponds to excess of oxygen vacancies. The relative intensities are sizably enhanced at the domain wall area (Fig. S2g–i). These quantified results confirm the accumulation of oxygen vacancies where the charged domain walls are created.



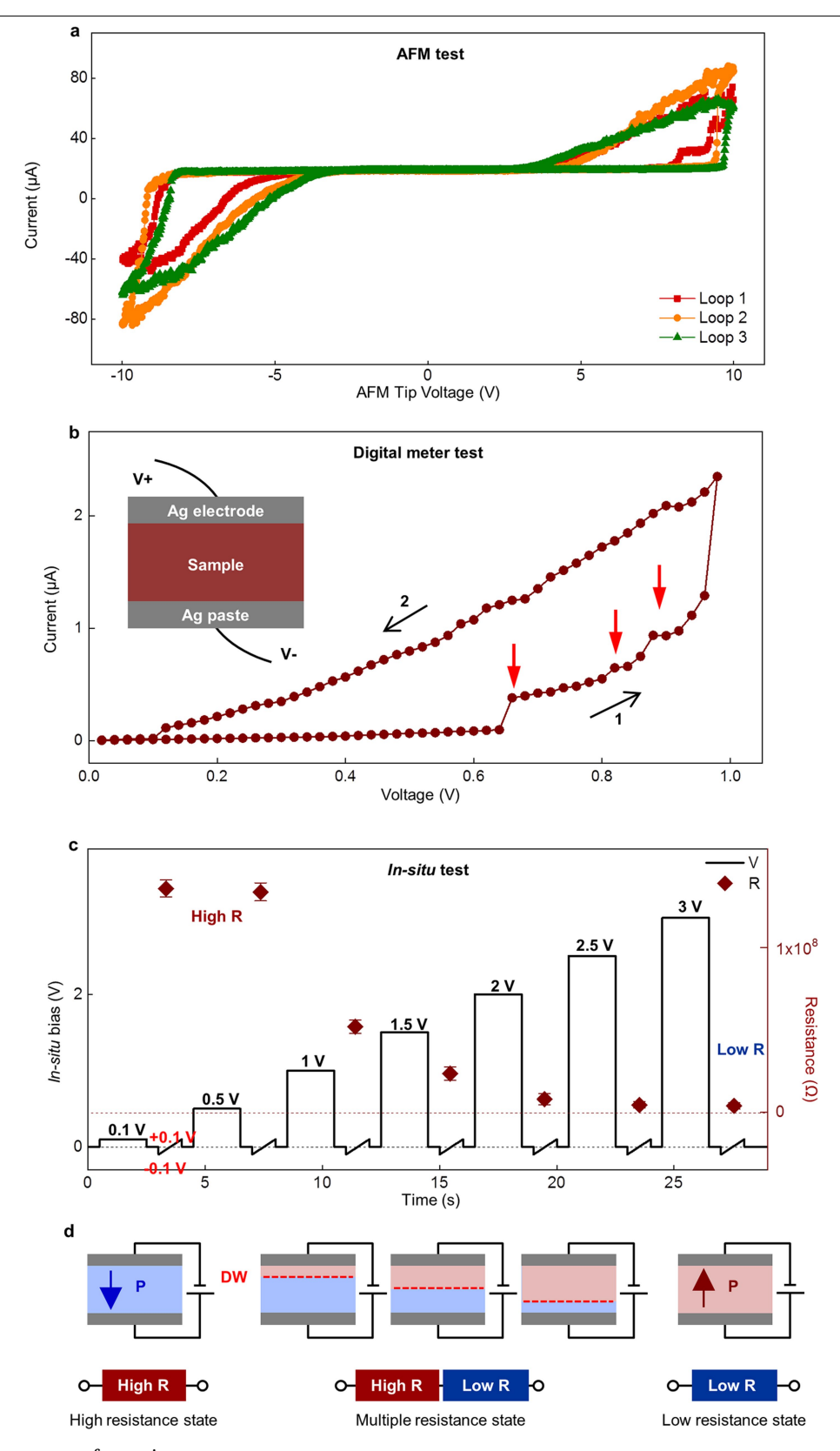
Extended Data Fig. 6 | Distortion of oxygen octahedron in BFO during domain-wall migration. a, The integrated differential phase contrast (iDPC) STEM image of the uniformly polarized state. Inset presents unit cell schemes with Bi, Fe, O, Sr, and Ruatoms (red, green, blue, yellow, and dark blue, respectively). Polarization vectors are presented by blue and red arrows at left. b, The iDPC-STEM image of "tail-to-tail" polarized state with schemes of atoms and polarization vectors. Scale bars (a,b), 1 nm. c, The distances of top and bottom oxygen atoms for each BFO layer in "tail-to-tail" state from experimental and calculation results. The error bars are the standard error of mean in each layer. d, The comparison of experiment and DFT calculation off-centre displacement of oxygen octahedra and Fe atoms for each BFO layer in "tail-to-tail" state. Off-center displacement is defined as a distance from the centre of oxygen octahedra (or Fe atoms) to the center of the Bi lattices. Along with the accumulation of oxygen vacancies, the distortion of oxygen octahedra in BFO is also observed. The positions of oxygen atoms are precisely determined using

iDPC-STEM imaging technique. Using a 4-quadrant detector, the iDPC-STEM imaging technique can observe both light and heavy elements with clear contrast. The light elements have a higher signal to dose ratio in iDPC imaging, which makes oxygen visible⁴³. In the tail-to-tail state, the distances between the top and bottom oxygen atoms are decreased at the domain wall, showing a clear compression of oxygen octahedra. Accompanied by the compression at the domain wall, oxygen octahedra at the BFO/SRO interfaces are stretched, leading to larger off-centre displacements. The lattice deformation across the domain wall is further confirmed by our DFT calculations (Fig. S7c,d), which demonstrate the quantitative agreement with experimental data. Previous works also indicated that missing oxygen atoms in perovskite unit cells lead to oxygen octahedra to be compressed^{44,45}. The observed lattice distortion and the accumulation of oxygen vacancies around the tail-to-tail domain wall are the structural and electrical factors for the creation and manipulation of charged domain wall, respectively.



Extended Data Fig. 7 | **DFT calculations of the atomic structure in different polarized states in SRO/BFO/SRO.** Fully relaxed atomic structure for single-domain structure (\mathbf{a} , \mathbf{b}) and tail-to-tail domain wall structure (\mathbf{c} , \mathbf{d}). V_o denotes the oxygen vacancy at the first (\mathbf{b}), second (\mathbf{c}), and central (\mathbf{d}) BiO layer. The arrows schematically denote the layer-resolved polarization and the length of arrows scales with the magnitude of displacements. When the uniform polarization state is sustained in 4-unit-cell BFO film, a tail-to-tail domain wall configuration is unstable. This behaviour changes when oxygen vacancies are deposited at the domain wall. Ionized oxygen vacancies provide a positive ionic

charge which screens the negative polarization charge at the tail-to-tail domain wall, resulting in a stable domain wall configuration. For the oxygen vacancy located in the first BiO monolayer from the interface, the atomic displacements near the oxygen vacancy are enhanced, but the BFO layer maintains a single domain structure. However, for the oxygen vacancy placed in the second or central BiO monolayer, the atomic displacements are pointing away from the oxygen vacancy layer, as expected from the positive charge of the ionized oxygen vacancy, forming a tail-to-tail domain wall structure.

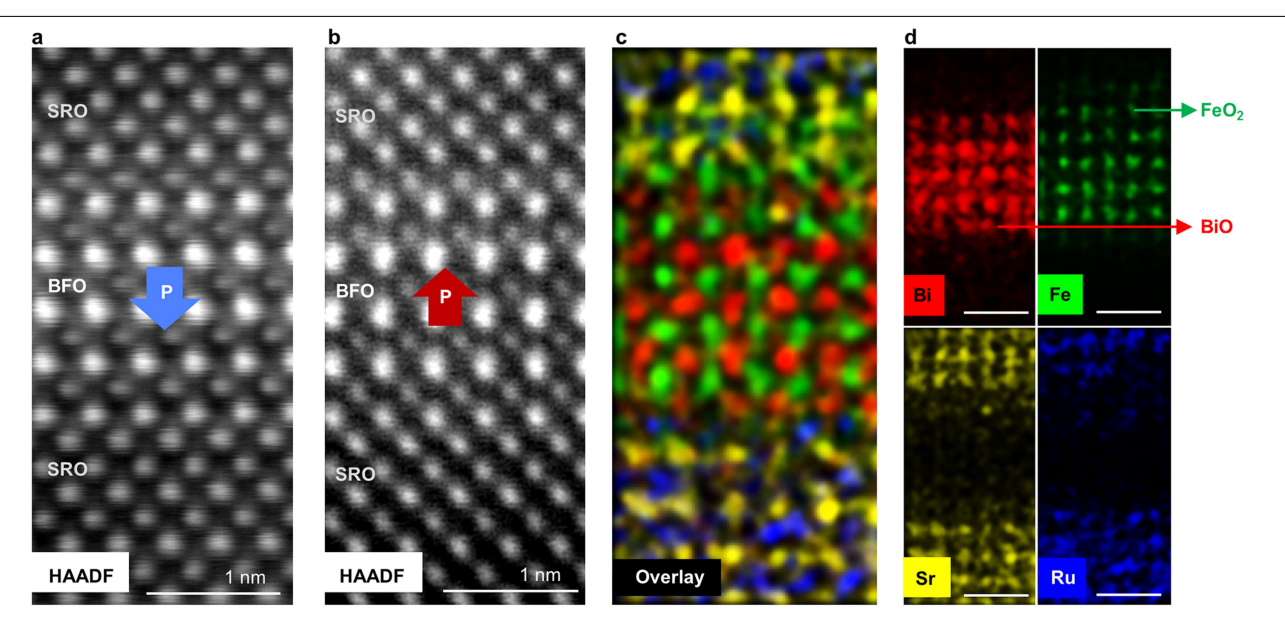


 $\textbf{Extended Data Fig. 8} | See \ next \ page \ for \ caption.$

Extended Data Fig. 8 | Measured current and resistance in SRO/BFO/SRO

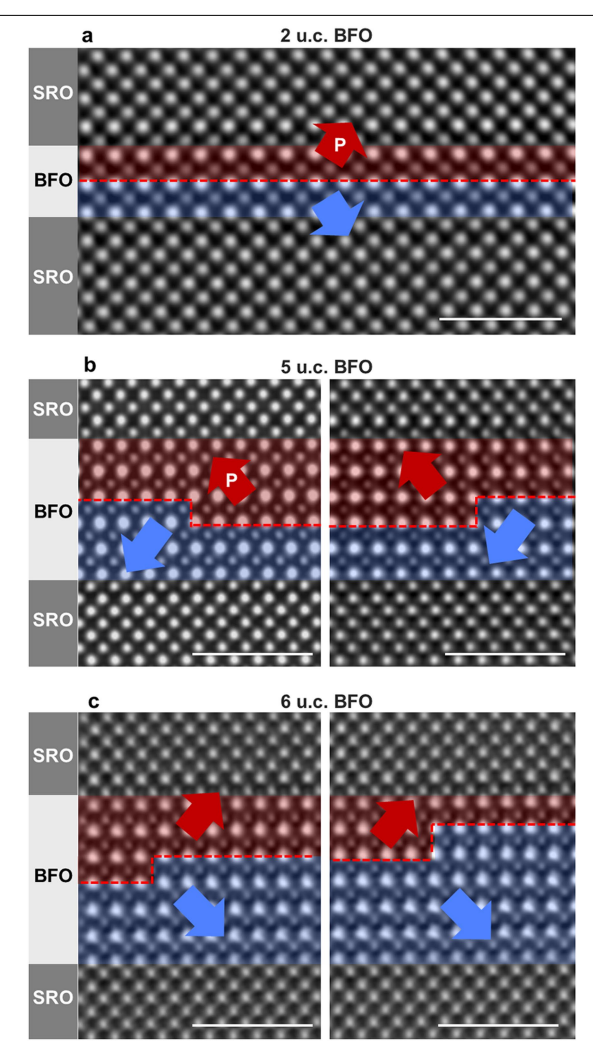
film. a, Current versus voltage curves measured by AFM on 4-u.c. SRO/BFO/SRO film, 0.5 V/s. Loops are displayed in chronological order. During the applied voltage cycles, I-V curves exhibit the pinched hysteresis character in memristor. **b**, Digital meter measurement in SRO/BFO/SRO film. The measured I-V curve using digital meter (details see below). The current exhibit jumps during positive sweeping, which are indicated by red arrows. Black arrows show the sweeping direction of voltages. Inset shows the diagram of measurement. **c**, The measurement of resistance during *in-situ* biasing process. The voltage-time curve illustrates the write and read voltage sequences for measurements of resistance. After applying the constant write voltage on film, the resistance is read between – 0.1 V and +0.1 V. Sketches of equivalent circuit diagrams for three typical polarization states are exhibited at **d**, corresponding to the high resistance state (High R), low resistance state (Low R) and intermediate states in R-V curves. The change of polarization states is discovered simultaneously

with the change of resistance in in-situ test, which is consistent with the in-situ imaging in Fig. 2a–c. The vertical I-V measurement is performed at room temperature. The bottom and surface electrodes of the sample are silver paste and a 50-nm-silver film (about 0.17 square millimeter in area) prepared by e-beam evaporation, respectively. The DC voltage across the contacts is applied to bias the sample, and then the current is measured by a digital meter (Keithley 2611B). The sweeping direction of the voltage is from positive to negative and finally returns to the initial state, e.g. from 0 volts to +1 volts to -1 volts and back to 0 volts. We choose AFM test, in-situ test and digital meter test to confirm the current and resistance character in BFO film. AFM probe measurement is used to examine the fine feature of I-V curve. In-situ probe measurement is used to examine the correspondence of resistance change and domain wall dynamic behavior. Digital meter measurement is used to examine the repeatability of I-V character in a large area of sample.

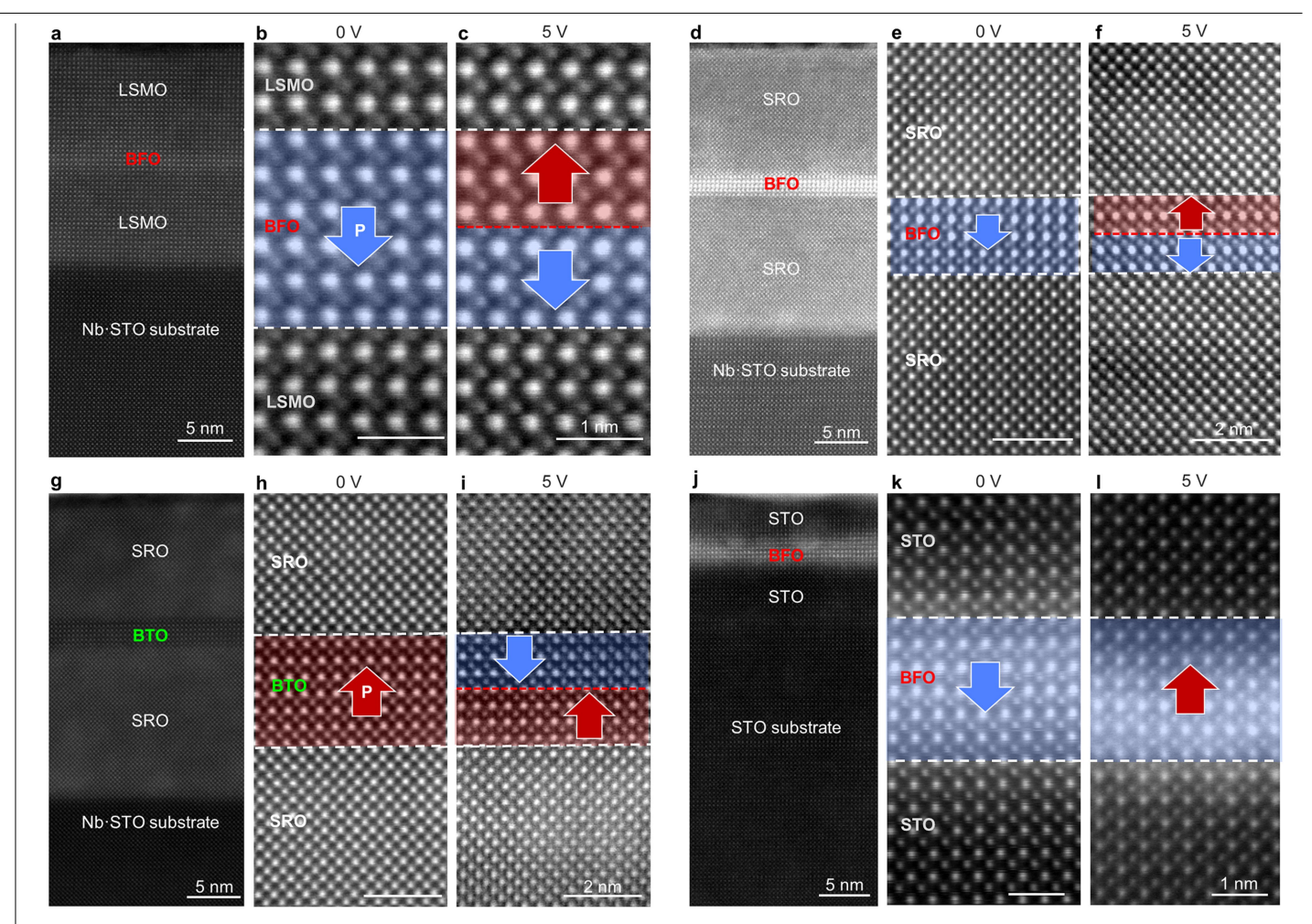


Extended Data Fig. 9 | **BFO films with asymmetric terminations. a-b**, The HAADF-STEM images of SRO/BFO/SRO film with asymmetric terminations. Film shows single domain states all the time under similar in-situ electric operation. c, The elemental EDX maps of (a,b) with false-colour overlaid on

Bi (red), Fe (green), Sr (yellow), and Ru (blue). The films have asymmetric terminations. In the upper SRO/BFO interface, the termination is FeO_2 , while the bottom interface shows BiO termination. Scale bars, 1 nm. Without the symmetric termination, BFO exhibits a uniform polarization.

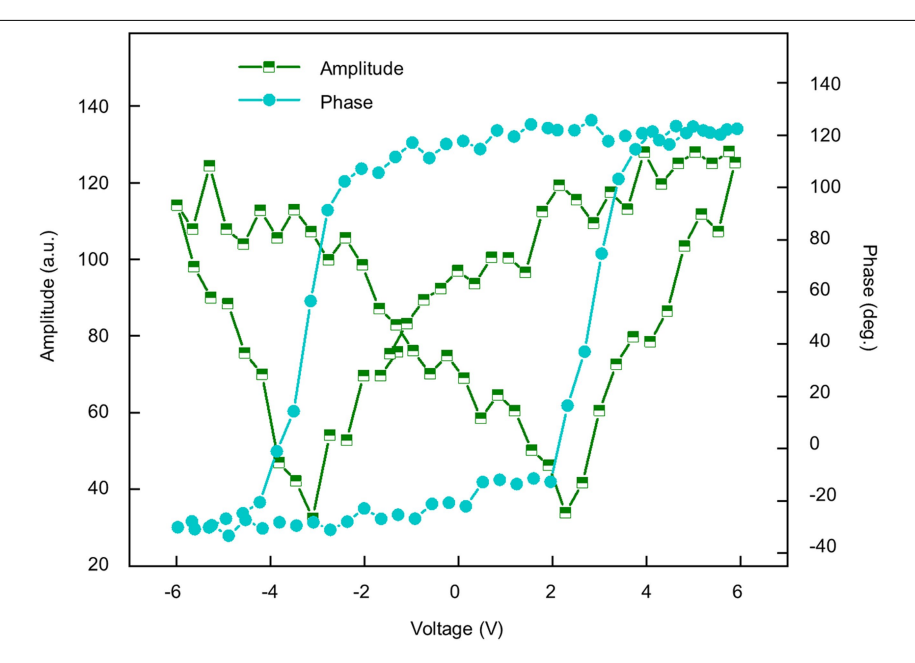


Extended Data Fig. 10 | BFO films with various thicknesses after applied voltage. a-c, HAADF images of 2-unit cells thick, 5-unit cells thick, and 6-unit cells thick BFO films, respectively. Domain wall (red dashed line) and polarization vectors (red arrows for polarized up and blue for polarized down) are superposed. Scale bars, 2 nm.



 $\label{eq:continuous} \textbf{Extended Data Fig. 11} | \textbf{Domain wall formation in different heterostructures.} \\ \textbf{a}, \mathsf{The magnified STEM image of La}_{0.7} \mathsf{Sr}_{0.3} \mathsf{MnO}_{3} / \mathsf{BiFeO}_{3} / \mathsf{La}_{0.7} \mathsf{Sr}_{0.3} \mathsf{MnO}_{3} (\mathsf{LSMO} / \mathsf{BFO}/\mathsf{LSMO}) \\ \mathsf{BFO}/\mathsf{LSMO}) \mathsf{structure.} \textbf{b}-\textbf{c}, \mathsf{The atomic-scale HAADF-STEM images of LSMO} / \mathsf{BFO}/\mathsf{LSMO} \text{ film at 0 V and 5 V, respectively.} \mathsf{The direction of polarization is} \\ \mathsf{marked by red and blue arrow.} \mathsf{Domain wall is marked by dashed red line.} \\ \mathsf{Interfaces are indicated by dashed white lines.} \mathsf{Scale bars, 1} \mathsf{nm.} \mathsf{BFO} \mathsf{shows} \\ \mathsf{uniform polarization at initial state.} \mathsf{After applying voltage of 5 volt, a tail-to-tail in-plane charged domain wall is found.} \\ \mathsf{d}, \mathsf{The magnified STEM image of SRO} / \mathsf{BFO}/\mathsf{SRO} \mathsf{structure with thick SRO electrodes.} \mathsf{The thickness of SRO electrode} \\ \mathsf{is more than 14 nm.} \textbf{e-f}, \mathsf{Atomic-scale HAADF-STEM images of SRO/BFO}/\mathsf{SRO} \\ \mathsf{film at 0 V and 5 V, respectively.} \mathsf{Scale bars, 2} \mathsf{nm.} \mathsf{A tail-to-tail in-plane charged} \\ \mathsf{domain wall is still formed when SRO electrodes become thicker.} \\ \mathbf{g}, \mathsf{The} \\ \\ \mathsf{SCALE} \mathsf{Compart of the thickness of SRO} \mathsf{Compart of the thickness} \mathsf{Compart of the thickness of th$

 $\label{eq:magnified} STEM image of SrRuO_3/BaTiO_3/SrRuO_3 (SRO/BTO/SRO) structure. \\ \textbf{h-i}, Atomic-scale HAADF-STEM images of SRO/BTO/SRO film at 0 V and 5 V, respectively. Scale bars, 2 nm. BTO shows uniform polarization at initial state. After applying voltage of 5 volt, a head-to-head in-plane charged domain wall is found. <math display="block">\textbf{j}, The \ magnified\ STEM \ image\ of\ SrTiO_3/BiFeO_3/SrTiO_3 (STO/BFO/STO) structure. \\ \textbf{k-l}, Atomic-scale\ HAADF-STEM \ images\ of\ STO/BFO/STO film\ at\ 0 V and\ 10 V, respectively. Interfaces\ of\ STO/BFO\ are indicated\ by\ dashed\ white lines. Scale\ bars, 1 nm. BFO\ is\ switched\ without\ charged\ domain\ wall\ after applying\ voltage\ of\ 10\ volt. Without\ conducting\ electrodes\ such\ as\ SRO\ and\ LSMO\ in\ film, BFO\ switches\ from\ the\ uniform\ polarization\ to\ the\ opposite\ without\ forming\ charged\ domain\ wall.$



 $\textbf{Extended Data Fig. 12} | \textbf{Ferroelectricity of SRO/4 u.c. BFO/SRO film.} \ Out-of-plane \ SS-PFM \ amplitude \ (half-filled olive \ square) \ and \ phase \ (filled \ blue \ circle) \ loop \ are measured in air.$